

Full length article

Enhanced inverse problem solution in angle-resolved scatterometry using a combination of library search and particle swarm algorithm



Dekun Yang^{a,1}, Wei Liang^{a,1}, Shizhao Wang^b, Wei Shen^c, Jiantao Zhou^{c,*}, Guanjun Wang^{a,*}, Chong Shen^{a,*}

^a School of Electronic Science and Technology, Hainan University, Haikou 570228, China

^b School of Power and Mechanical Engineering, Wuhan University, Wuhan 430072, China

^c The Institute of Technological Sciences, Wuhan University, Wuhan 430072, China

ARTICLE INFO

Keywords:

Angle-resolved scatterometer
Inverse problem solution
Library search
Particle swarm optimization

ABSTRACT

The angle-resolved scatterometer (ARS) is a model-based technique that has demonstrated significant potential for critical dimension (CD) measurements in integrated circuit (IC) manufacturing due to its high speed, accuracy, and non-contact operation. ARS is essentially an inverse problem-solving process. Traditional methods, such as library search, rely on extensive spectral databases with fine grid intervals, which impose substantial storage and computational demands. Nonlinear regression techniques, like the Levenberg-Marquardt (LM) algorithm, require significant computational resources for real-time Jacobian matrix evaluations, limiting their applicability for online measurements. To overcome these challenges, we propose a hybrid method combining library search and particle swarm optimization (LSPSO). This approach employs a sparse spectral library with large grid intervals (LGI), dramatically reducing storage requirements. The LGI library also guides the initial search direction for the PSO, eliminating the need for early model evaluations and improving computational efficiency by reducing the number of model computations. Simulations on both single-parameter (film) and multi-parameter (grating) models demonstrate the accuracy of LSPSO, with noise analysis further confirming its stability. Experimental validation on grating structures reveals that LSPSO improves computational efficiency by 52% compared to standard PSO and operates 1.7 times faster than the LM method. Moreover, the spectral data required by LSPSO is reduced to just 0.1% of the data needed by traditional library search methods. These results position LSPSO as a highly efficient, accurate, and resource-efficient solution for CD measurements in ARS applications.

1. Introduction

Optical scatterometry is a model-based technique that enables the characterization of nanostructures below the diffraction limit [1,2]. Compared to traditional optical methods, it offers non-contact and high-speed measurements [3], making it widely used for critical dimension (CD) characterization in the integrated circuit (IC) industry [4–7]. Scatterometers are typically classified into two types based on their measurement variables: spectral-resolved and angle-resolved [8]. Angle-resolved scatterometers (ARS) capture optical responses by adjusting incident or detection angles, unlike spectroscopic scatterometers, which scan across continuous wavelengths. In ARS, obtaining the refractive index at a single wavelength is usually sufficient [9]. With high

numerical aperture (NA) objectives, ARS also overcomes challenges in rotational measurements [10–12], offering greater flexibility than spectral-resolved scatterometers. ARS comprises two main components: forward modeling and inverse structure retrieving [13]. In the forward process, electromagnetic solvers such as finite-difference time-domain (FDTD) [14], finite element method (FEM) [15], and rigorous coupled-wave analysis (RCWA) [16–19] are used to determine diffraction efficiency. Other rigorous or approximate computational methods [20–24] are listed in Table 1.

In semiconductor manufacturing, the inverse problem is commonly addressed using the library search method, which relies on a pre-generated spectral library [25–27]. Measured spectra are compared to the library entries, and the parameters of the best-matching spectrum

* Corresponding authors.

E-mail address: chongshen@hainanu.edu.cn (C. Shen).

¹ Dekun Yang and Wei Liang contributed equally to this work.

Table 1

Supplementary methods in forward and inverse process of optical scatterometry.

The solvers in forward process	Solution methods	The algorithms in inverse problems
Boundary integral equation [20]	Rigorous computation	Bat algorithm [39]
Boundary element method [21]		Forward propagation network [40]
Differential method [22]		Seagull optimization algorithm [41]
Chandezon method [23]		Exponential-trigonometric algorithm [42]
Approximate computational Method [24]	Approximate computation	Wavelet transforms algorithm [43,44] Optimized neural network [45] YUKI algorithm [46]

are taken as the result. However, this approach creates challenges in storage and accuracy, as large libraries, often containing millions of spectra for multi-parameter samples, are required. Researchers have refined the traditional method by incorporating interpolation and correction techniques to improve search precision [28,29], though system noise can still introduce instability. Zhu et al. proposed a hybrid algorithm combining heuristic search with Gauss-Newton iteration [30], but it requires initial parameters close to the global solution, increasing both time and storage demands for library generation.

Nonlinear regression [31,32], particularly the Levenberg-Marquardt (LM) algorithm, is another popular approach to solving inverse problems in optical scatterometry [33,34]. To enhance accuracy and efficiency, LM has been combined with artificial neural networks or library search methods [35], and optimizations have been made to the objective function and regularization coefficients [36]. However, the LM algorithm relies on gradient descent and requires time-consuming Jacobian matrix calculations [13]. Reducing computational time for nonlinear regression remains a significant challenge. Direct optimization algorithms, such as particle swarm optimization (PSO), offer a potential solution by being independent of analytical expressions [37,38], though they often lack guided search direction and may fall into local optima

due to randomly generated initial parameters. Other advanced optimization algorithms are under development and may provide future solutions for scatterometry (as shown in Table 1.) [39–46]. Nonetheless, methods like neural networks and machine learning, which require large sample datasets for training, remain limited in their application to scattering measurements.

This study proposes a method combining library search and particle swarm optimization (LSPSO) to address the challenges mentioned above. The spectral library is generated using a large grid interval (LGI), significantly reducing storage requirements. Unlike nonlinear regression, the PSO algorithm directly performs optimization, avoiding complex Jacobian matrix calculations. Additionally, the LGI library guides the PSO's initial search direction, reducing the number of RCWA model computations. In summary, LSPSO offers a novel approach to reduce storage and computation time. The effectiveness of the algorithm is validated using Si-based SiO₂ thin film and Si₃N₄ grating models, with experimental verification on a Si nano-grating structure. Results show that LSPSO requires only 0.1 % of the spectral data used by traditional library search methods for the same accuracy, improving solving efficiency by 52 % compared to PSO and being 1.7 times faster than the LM method with the LGI library.

2. Method

2.1. Overview of the LSPSO method

The flowchart of the combined algorithm LSPSO for solving inverse problems is depicted in Fig. 1. For an ARS instrument, the measured spectrum is based on the variation of reflectance with incident angles. Consequently, the reflectance is defined as a K -dimensional vector $Y = [Y_1, Y_2, \dots, Y_K]$, where K represents the number of data points within the range of incident angles. The theoretical reflectance $Y^{\text{theory}} = [Y^{\text{theory}}_1, Y^{\text{theory}}_2, \dots, Y^{\text{theory}}_K]$, obtained through an electromagnetic solver, serves as a reference to the measured reflectance. In this study, a self-developed RCWA model implemented in the MATLAB environment was employed for the calculations. The reflectance is mutually mapped with the nanoscale structure vector $X = [X_1, X_2, \dots, X_N]$, where N denotes the number of measured parameters. The objective of the LSPSO

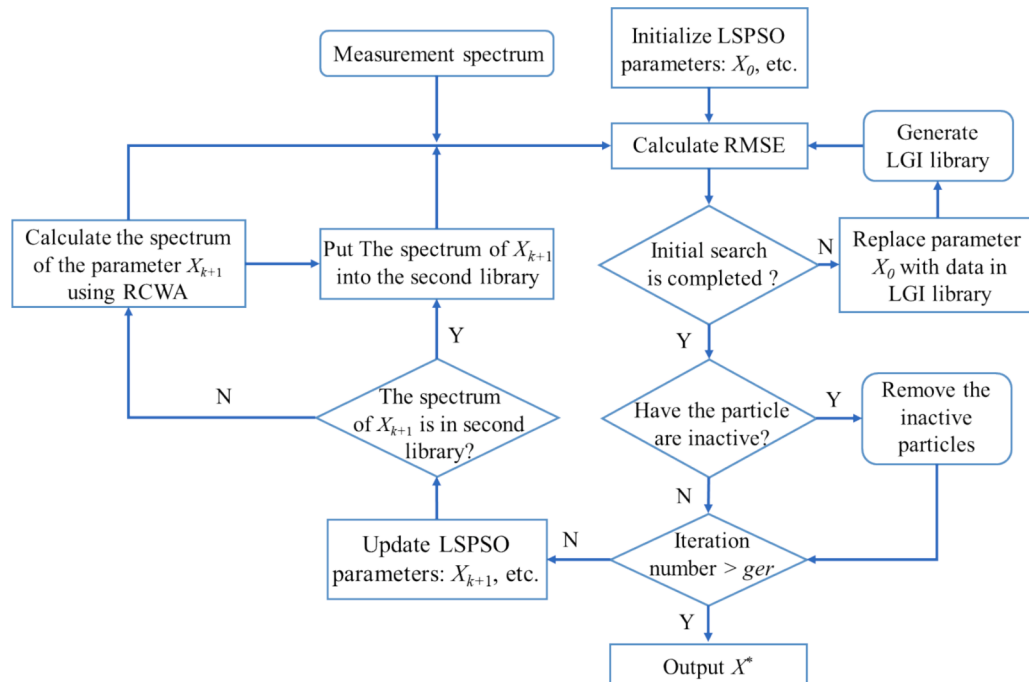


Fig. 1. Overview of the proposed LSPSO method.

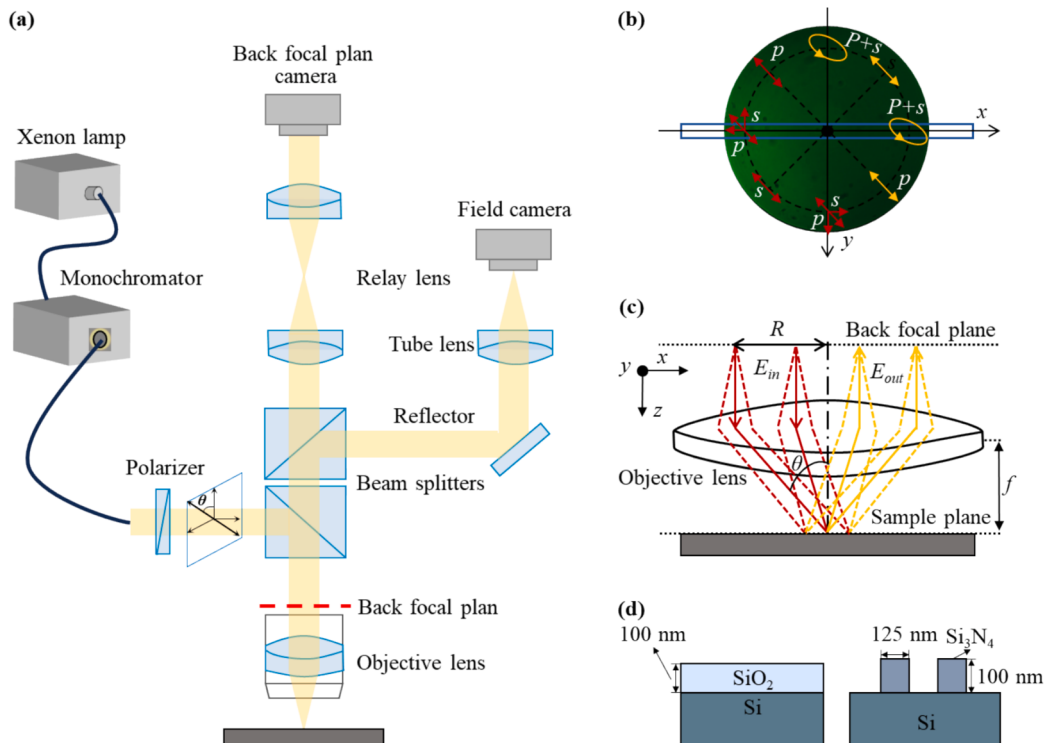


Fig. 2. The measurement principle of angle-resolved scatterometry device. (a) hardware configuration; (b) the incident and reflected beams exhibit distinct changes in polarization, where the incident beam is denoted in red, and the reflected beam is denoted in yellow; (c) the relationship between the BFP radius R and incident angle θ ; (d) Si-based SiO₂ films and Si₃N₄ grating model.

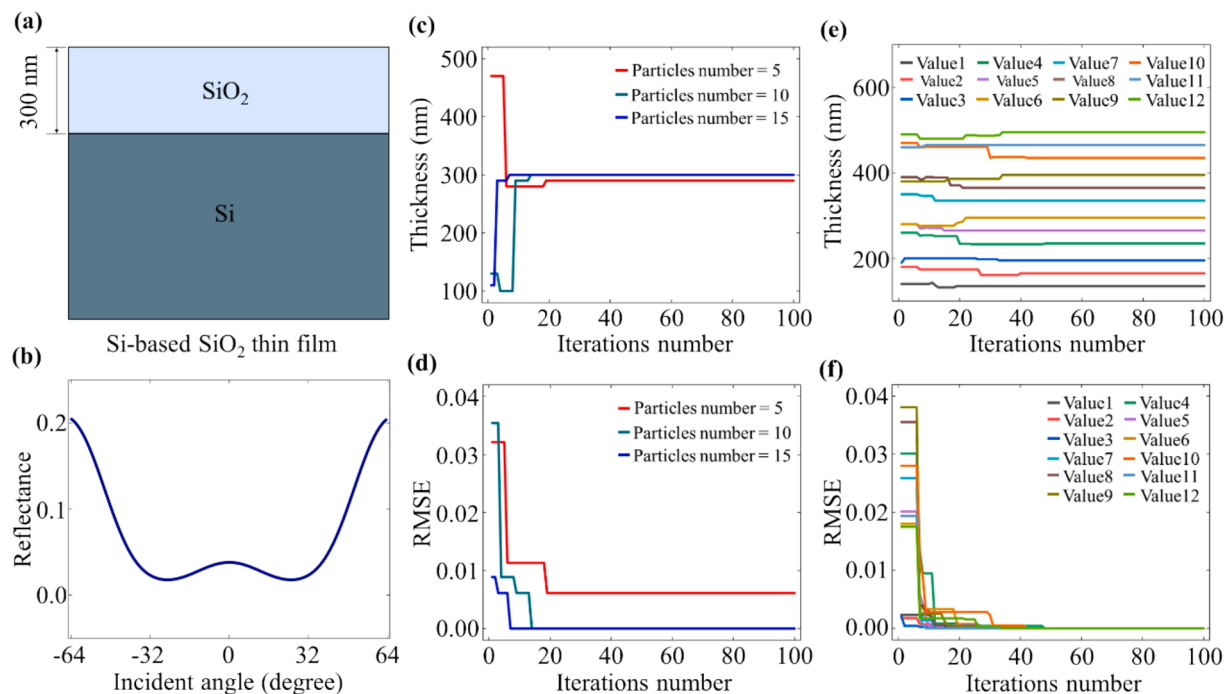


Fig. 3. The process of solving a single-parameter thin film model using the LSPSO algorithm. (a) the film model of 300 nm thickness; (b) angle-resolved reflectance of 300 nm thickness; (c) convergence process of 300 nm thickness under different particle numbers; (d) RMSE corresponding to different particle numbers; (e) convergence process for 12 thickness values; (f) RMSE corresponding to 12 thickness values.

algorithm is to search for the minimum difference between Y and Y^{theory} , hereby extracting the expected parameter X^* . The difference level is assessed through the computation of the root mean square error (RMSE), which is a commonly employed method in optical scatterometry.

Therefore, the extracting process of X^* is represented as follows:

Table 2

Detailed parameters of the film model and PSO.

Substrate	Film	Measure wavelength	Incident angle range	Film thickness	LGI library scope	Grid interval
Si Particles number 5, 10, 15	SiO ₂ Max iterations number 100	644 nm <i>w</i> 0.8	-64.2°–64.2° <i>c</i> ₁ , <i>c</i> ₂ 0.5, 0.5	300 nm <i>r</i> ₁ , <i>r</i> ₂ Random in [0, 1]	250 nm–350 nm <i>x</i> _{lim} 250 nm–350 nm	10 nm <i>v</i> _{lim} [-10, 10]

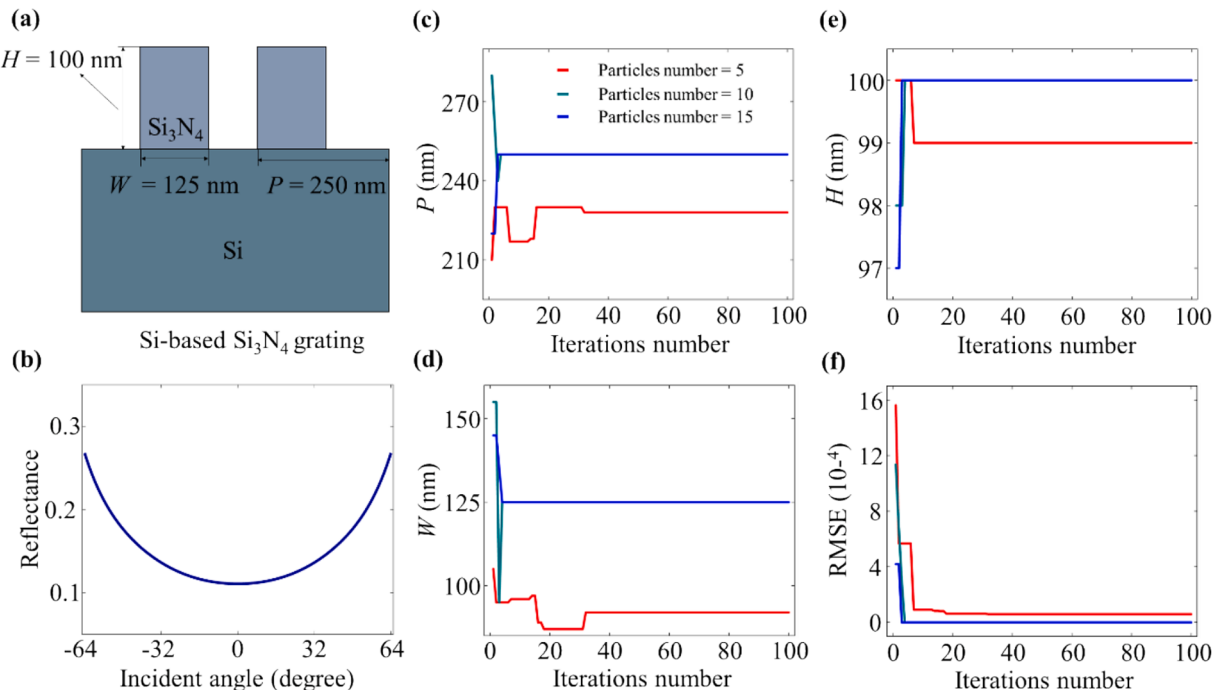


Fig. 4. The process of solving a multi-parameter grating model using the LSPSO algorithm. (a) the grating model with true values of $P = 250$ nm, $H = 100$ nm, and $W = 125$ nm; (b) angle-resolved reflectance of the true values grating; (c) convergence process of P parameter under different particle numbers; (d) convergence process of W parameter under different particle numbers; (e) convergence process of H parameter under different particle numbers; (f) RMSE corresponding to true values grating.

Table 3

Parameter ranges and LGI library design scheme for the grating.

Parameters	True values (nm)	The range of LGI (nm)	Step (nm)	Spectra number
P	250	200–300	10	11
H	100	50–150	10	11
W	125	75–175	10	11

$$X^* = \operatorname{argmin}_X \left\{ \sqrt{\frac{1}{K} \sum_{i=1}^K [Y_i - Y_i^{\text{theory}}(X)]^2} \right\} \quad (1)$$

To address storage limitations, the spectral library is constructed using a sparse grid interval via the LGI library, instead of the traditional dense grid approach. Additionally, the parameter extraction process employs the direct optimization algorithm, PSO, which eliminates the need for spectral analytical expressions typically required in nonlinear regression methods. The integration of the LGI library with PSO effectively mitigates the limitations of both traditional library search methods and nonlinear regression techniques. The procedure for LSPSO is outlined as follows.

Step1: Generate an LGI library. The spectra in the LGI library consist of angle-resolved reflectance data Y , which are obtained through self-developed RCWA model. Each reflectance data corresponds to a specific size parameter vector X . Within the empirical error range of the

design dimensions, the vector X is determined with a larger step size.

Step2: Initialize the parameters of PSO and conduct initial search. The initial dimensional parameter X_0 will be replaced by X in LGI library, based on the criterion of minimum difference between the X and X_0 . The initial search is considered complete when all particle parameters X_0 have been updated in PSO process.

Step3: Assess the particle activity. If the initial search is completed, particle activity is determined and particles below the activity threshold are removed.

Step4: Calculate RCWA model. The initial search process in the previous step provides a rough direction for the PSO. The further optimization is achieved by real-time invocation of the RCWA model. The reflectance data generated by RCWA simulation is added to the second library. When the same position is encountered in subsequent searches, there is no need to repeatedly call the RCWA model for calculations.

Step5: Calculate the RMSE. The measured spectrum Y and the simulated spectrum Y^{theory} are employed as inputs to calculate the fitness function RMSE. This serves as the basis for particle updates in the subsequent iteration process.

Step6: Update the parameters of PSO. If the target number of iterations n has not been reached, the particle's X_0 and other parameters are updated.

Step7: Extract expected parameter X^* . The process of RCWA model calculation and particle updates is repeated until the stopping criteria are met, and the expected parameter X^* is outputted.

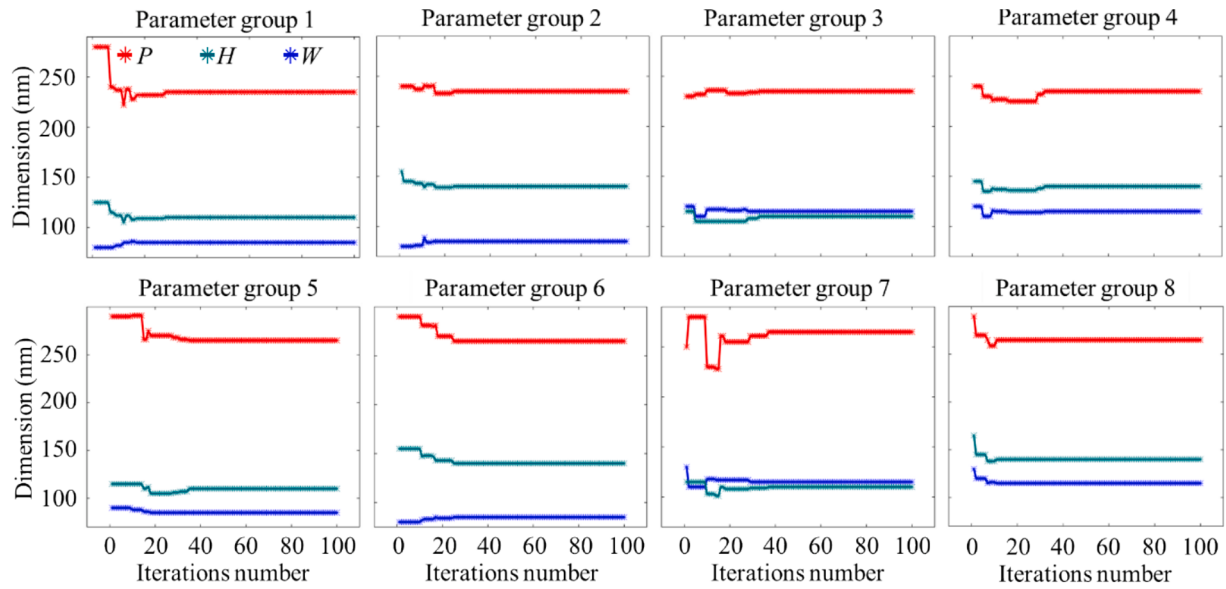


Fig. 5. Convergence process of grating parameter groups.

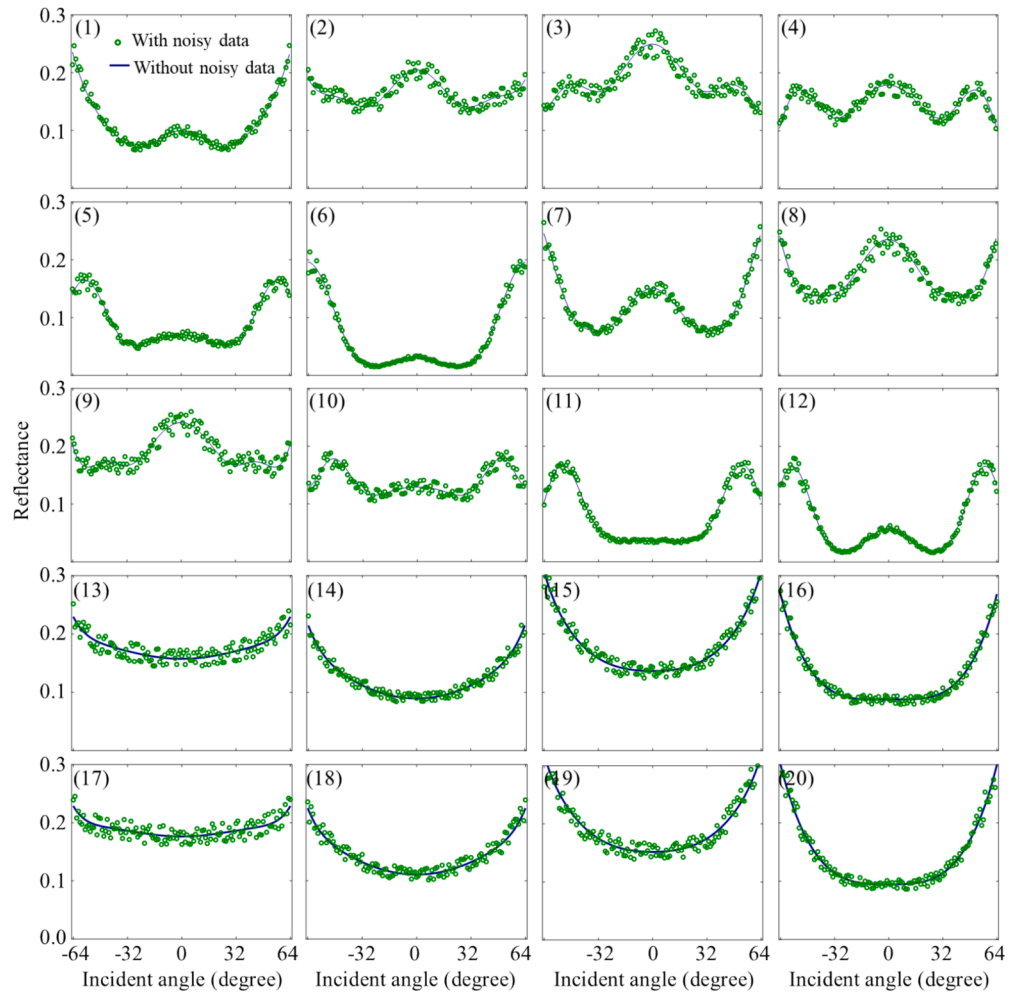


Fig. 6. The reflectance with noisy data for the 12 film and 8 grating values: (1)-(12) are thin films, (13)-(20) are gratings.

2.2. PSO algorithm

The PSO algorithm was initially proposed by James Kennedy and

Russell Eberhart in 1995 [47] and has since undergone further development [38,48–50]. Its core concept is to simulate the collective movement patterns of a flock of birds to search for optimal solutions to

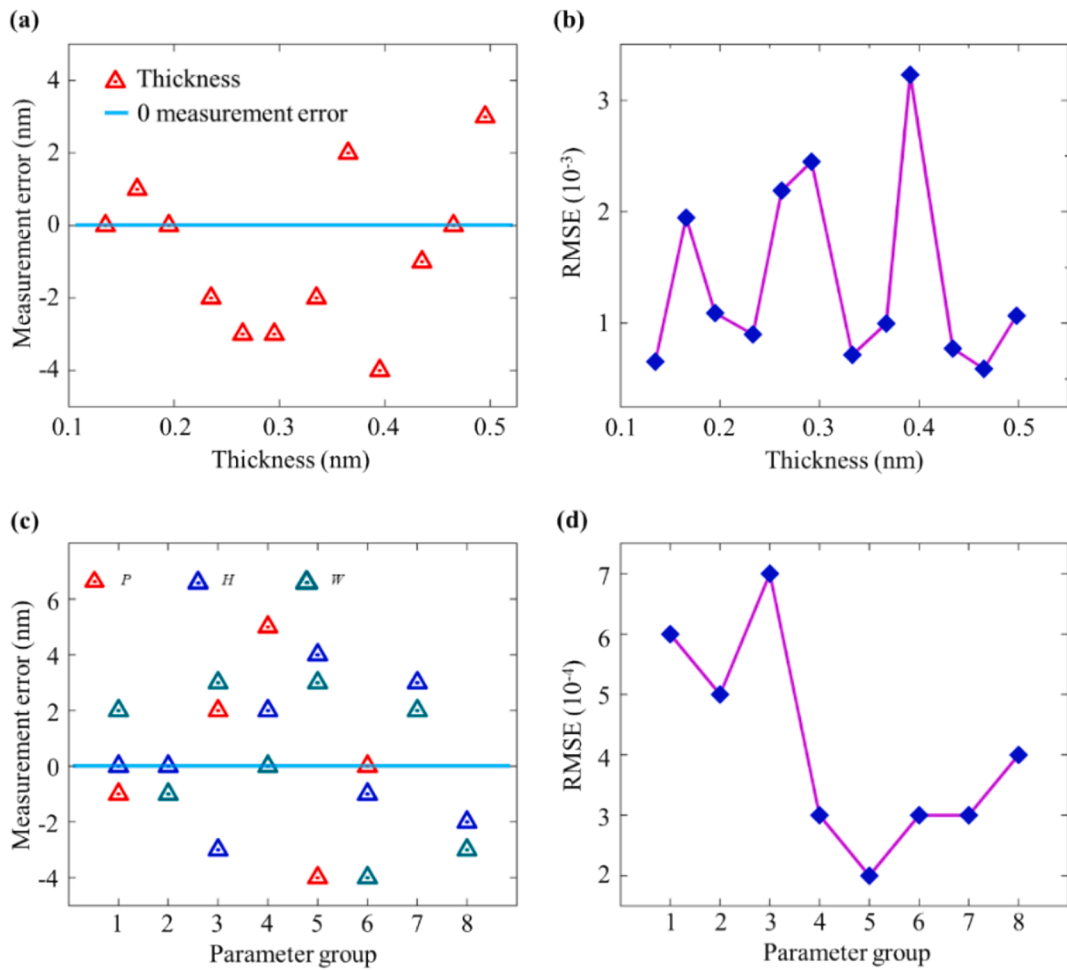


Fig. 7. The measurement results with noisy data. (a) the measurement error of different film thicknesses; (b) the RMSE of different film thicknesses; (c) the measurement error of different grating parameters; (b) the RMSE of different grating parameters.

problems. PSO has been widely applied in various engineering and scientific research domains [51–53]. To the best of our knowledge, this is the first application of PSO for solving inverse problems in optical scatterometry.

The PSO algorithm follows a search process in the solution space, where a certain number of solutions (particles) are randomly generated and assigned initial velocities. Each particle traverses a specific path in the space, where each position represents a potential solution within the search space. Each particle's position x_{id} is influenced by the following factors:

- a) Personal best position ($pbest_{id}$) of the particle.
- b) Global best position ($gbest_{id}$) of the particle swarm.
- c) Current velocity (v_{id}) of the particle.

In PSO, the velocity and position of each particle change according to the following equations:

$$v_{id}^{k+1} = wv_{id}^k + c_1 r_1^k (pbest_{id}^k - x_{id}^k) + c_2 r_2^k (gbest_{id}^k - x_{id}^k) \quad (2)$$

$$x_{id}^{k+1} = x_{id}^k + v_{id}^{k+1} \quad (3)$$

where v_{id} and x_{id} respectively represent the current velocity and position of the i th particle in the d -dimensional space. The $pbest_{id}$ and $gbest_{id}$ denote the best personal and best global position, respectively. The parameter w represents the inertia weight associated with the particle's previous position, while c_1 and c_2 are the acceleration constants. The r_1 and r_2 are random numbers within the range 0–1.

The procedure of the PSO is described in detail as follows:

Step1: Set PSO parameters:

a) Sample-related parameters: sample parameter dimension d , position constraint x_{lim} , velocity constraint v_{lim} .

b) PSO-related parameters: number of particles n , maximum iteration count ger , inertia weight w , self-influence factor c_1 , and swarm-influence factor c_2 . Randomly generate the initial position x_{id} and initial velocity v_{id} of the particle.

Step2: Update PSO parameters. Initially, compute the RMSE between the Y and Y^{theory} . Based on the RMSE value, identify the personal best $pbest$ and global best $gbest$. Subsequently, update the x_{id} and v_{id} of the PSO using the formulas 1 and 2.

Step3: Determine the quality of PSO parameters. Evaluate the quality of the particle by examining the particle's velocity and position. If the velocity or position exceeds the predefined limits (v_{lim} and x_{lim}), discard the particle. Furthermore, perform an activity analysis on the particles and remove those with velocities below the activity threshold. By employing quality assessment, it is possible to reduce the iterations involving low-quality particles, thereby minimizing the number of RCWA computations.

Step4: Stop the PSO process. The particles repeat steps 2–3 iteratively until the termination criteria are met. The stopping criteria typically consist of the maximum number of iterations or a fitness threshold.

3. Results

3.1. Experimental setup principle

The schematic diagram of the constructed ARS device is presented in

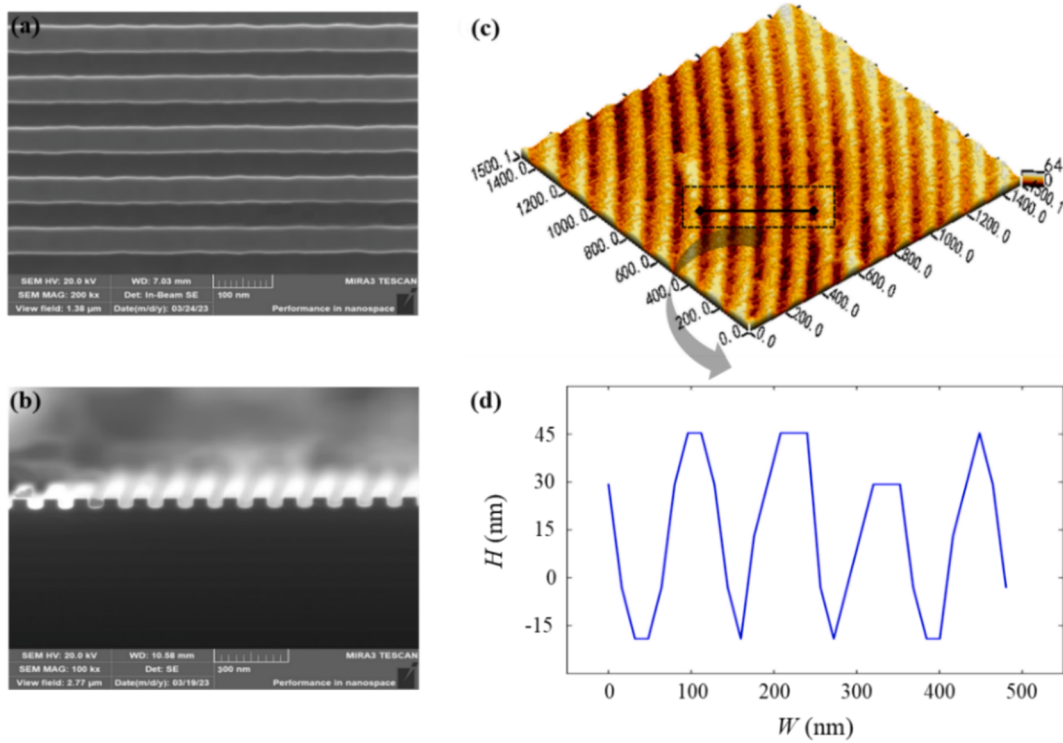


Fig. 8. Characterization of rectangular Si grating. (a) SEM Top-View; (b) SEM Cross-Section; (c) AFM 3D Profile; (d) AFM cross-section line example.

Fig. 2a. It comprises four main components: the illumination optical path, the sample back focal plane (BFP) unit, the measurement optical path, and the positioning optical path. A broadband xenon lamp white light source is connected to a monochromator and coupled into the system through an optical fiber. The monochromator filters the light from 200 to 2000 nm to produce monochromatic light. A thin film linear polarizer is mounted in a rotatable mechanical cardan ring, allowing the selection of linearly polarized light at any desired angle. The linearly polarized light passes through a beam splitter and an objective lens to illuminate the sample at different incident angles. The system employs a 100 \times high magnification objective lens (EC Epiplan-Neofluar from ZEISS, Jena, Germany) with a NA of 0.9. The output spot size from the fiber is slightly larger than the entrance pupil of the objective lens. This ensures NA is fully utilized in the measurement. Subsequently, the BFP image containing angle information of the samples is captured through the measurement optical path. In certain cases, precise localization of the measurement region is essential. Visual localization is achieved by employing a field camera to receive the object image of the objective lens.

For the ARS device, the high NA objective lens enables the acquisition of angle-resolved reflectance data in a single measurement. As measured on the bare silicon wafer depicted in Fig. 2b and c, the polarization state of the incident light in BFP varies with the incident angle θ and azimuthal angle φ . Each point of the BFP corresponds to a unique θ and φ . The θ range is determined by the NA of the objective lens, and the maximum incident angle θ_{\max} is defined as:

$$\theta_{\max} = \sin^{-1}(\text{NA}) \quad (4)$$

Therefore, for a 0.9NA objective, the achieved θ_{\max} is 64.16°. In ARS, the measured angle-resolved reflectance needs to be normalized with a reference standard sample. This performed normalization is to facilitate the comparison with the reflectance calculated by the RCWA model. The normalization process is described as follows:

$$R_{\text{sam}} = I_{\text{sam}} * \frac{R_{\text{the}}}{I_{\text{ref}}} \quad (5)$$

where R_{sam} is the measured target sample reflectance, I_{sam} is the intensity of the target sample in CCD, R_{the} is the theoretical reflectance of the reference standard sample, and I_{ref} is the measured intensity of the standard sample. To minimize measurement errors, it is crucial to eliminate the glare I_{gla} in the microscope and the dark current of the CCD. This can be accomplished by subtracting the BFP image without sample from the sample BFP image. Then sample reflectance is stated as:

$$R_{\text{sam}} = (I_{\text{sam}} - I_{\text{gla}}) * \frac{R_{\text{the}}}{I_{\text{ref}} - I_{\text{gla}}} \quad (6)$$

3.2. Simulation results

In this section, the accuracy of the LSPSO algorithm is validated using the Si-based SiO₂ thin film and Si₃N₄ grating model as depicted in Fig. 2d. First, the sensitivity operator previously proposed in our research [54] is used to select the sensitive measurement wavelength. Specifically, the derivative (referred to as sensitivity) of the reflectance is continuously computed along multiple variable directions. Then, the sum of sensitivities in the remaining variable directions within the measurement wavelength range is calculated. A larger sum of sensitivities indicates higher sensitivity of the model parameters at that measurement wavelength. For the SiO₂ thin film model, the model parameters include the film thickness and the incident angle. For example, at a true film thickness of 300 nm (as shown in Fig. 3a), the corresponding angle-resolved reflectance is depicted in Fig. 3b. The spectra in LGI library of the LSPSO are generated within the range of 250 nm-350 nm with a spacing of 10 nm. The sensitivity operator indicates that the most sensitive measurement wavelength within this range is 544 nm.

The detailed configuration of the parameters of the model and PSO is presented in Table 2. The variation of optimization results with respect to the number of iterations is illustrated in Fig. 3c. The optimization process varies with the number of particles; however, the initial search direction stabilizes after a few iterations. When the number of particles is small (5 particles), the optimization tends to get trapped in local

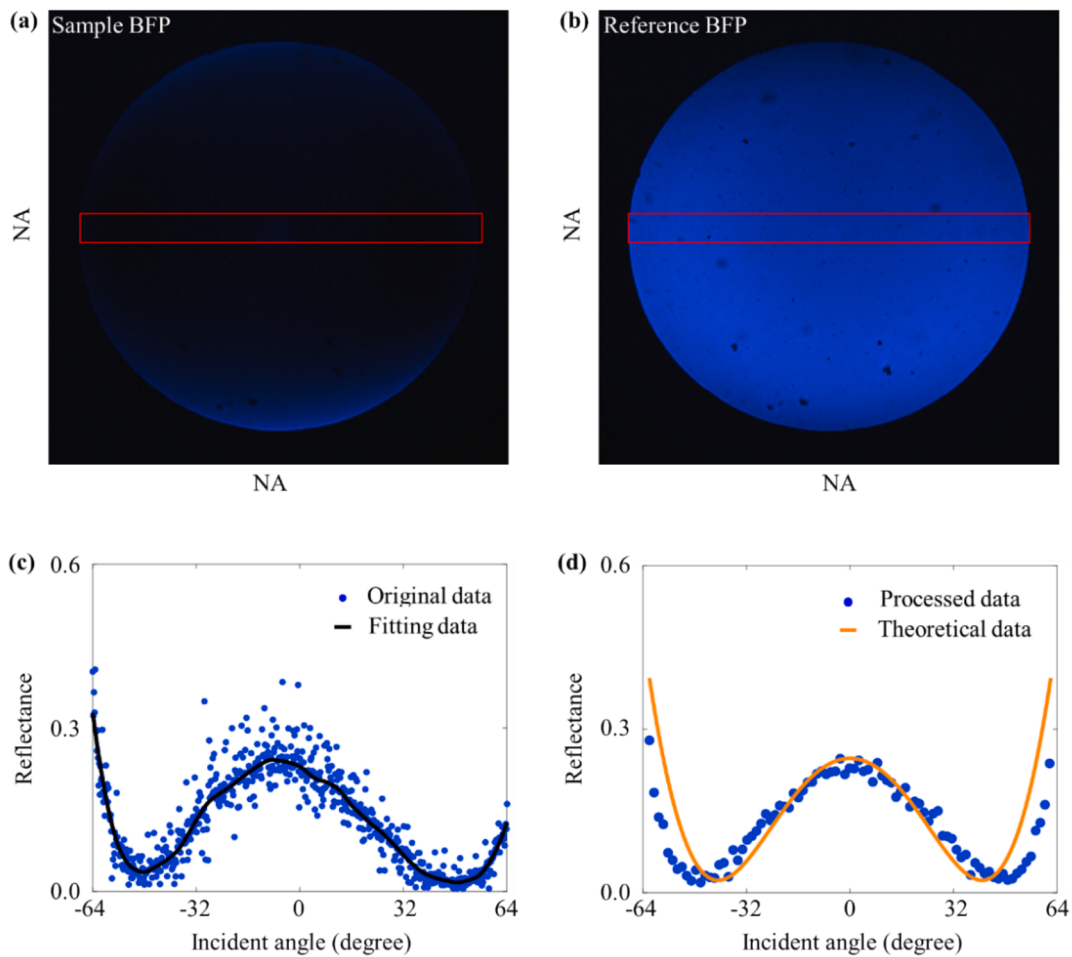


Fig. 9. Measurement results of Si grating. (a) measured sample BFP; (b) measured reference BFP; (c) normalized reflectance; (d) comparison of solved reflectance and measured reflectance; measured grating dimensions: $P = 124 \text{ nm}$, $H = 65 \text{ nm}$, $W = 64 \text{ nm}$.

minima (290 nm). However, as the number of particles increases to 10 and 15, the algorithm is able to find the true value of 300 nm within fewer iterations. Increasing the number of particles shortens the initial search process based on the LGI library, that is, the stage where the film thickness value does not change in the initial iteration. With 5 particles, LSPSO takes 5 iterations to complete the initial search, while increasing the number of particles to 10 reduces the iteration number to 3. Similarly, increasing the number of particles can shorten the convergence time for film thickness. However, once the number of particles is sufficient to find the global optimum, further increasing the particle number does not significantly reduce the search time of the LGI library, as observed when the particle number increases from 10 to 15. The variation of RMSE during the search process for different numbers of particles is illustrated in Fig. 3d.

To validate the stability of the LSPSO algorithm in solving single-parameter problems, an additional simulation scheme was designed with true film thickness values and LGI libraries. LGI library data were generated at 10 nm intervals within the film thickness ranges of 100 nm–200 nm, 200 nm–300 nm, 300 nm–400 nm, and 400 nm–500 nm. The corresponding true film thickness values selected within these ranges are (135 nm, 165 nm, 195 nm), (235 nm, 265 nm, 295 nm), (335 nm, 365 nm, 395 nm), and (435 nm, 465 nm, 495 nm), respectively. A total of 12 true film thickness values not included in the LGI library were chosen for inversion solving. The variation of these 12 film thickness values during the iterative process is shown in Fig. 3e. Within 50 iterations, all true values were solved with 100 % accuracy. The RMSE variation of each film thickness value during the iterations is depicted in Fig. 3f, with the final fitness function converging to 0.

The actual measured structure parameters are typically multiple, necessitating the validation of the LSPSO algorithm for multi-parameter solving. As shown in Fig. 4a, the Si_3N_4 grating model on an Si substrate, the measurement parameters include period P , height H , and width W , with true values of 250 nm, 100 nm, and 125 nm, respectively. Fig. 4b shows the angular-resolved reflectance of the grating. Similar to film thickness, when the number of particles reaches 10, the grating parameters can be solved with 100 % accuracy. To verify the stability of LSPSO in multi-parameter measurement, the LGI library generation scheme listed in Table 3 was designed. Two true value points were selected from the size range of each parameter: [235 nm, 265 nm], [85 nm, 115 nm], and [110 nm, 140 nm]. These three parameters were combined into 8 different grating structures, sequentially numbered as parameter groups 1–8. For the multi-parameter solution, it was found that employing 30 particles did not fully ensure the accuracy of all parameter groups. Increasing the particle count to 50 effectively enhanced the stability of the solution. Therefore, the number of particles was set to 50 for solving the 8 parameter groups.

The variation of the 8 parameter groups during the iterative process is shown in Fig. 5. Compared to single-parameter film solving, the initial search guided by the LGI library is increased in number, requiring dozens of iterations to determine the optimal search direction. This is primarily due to the multi-dimensional nature of the multi-parameter solution space, necessitating more iterations to explore the parameter groups. Similarly, the process of searching with the RCWA model is also extended, with most parameters requiring more than 30 iterations to converge to the true values. The validation using both single-parameter (film) and multi-parameter (grating) structures demonstrates the LSPSO

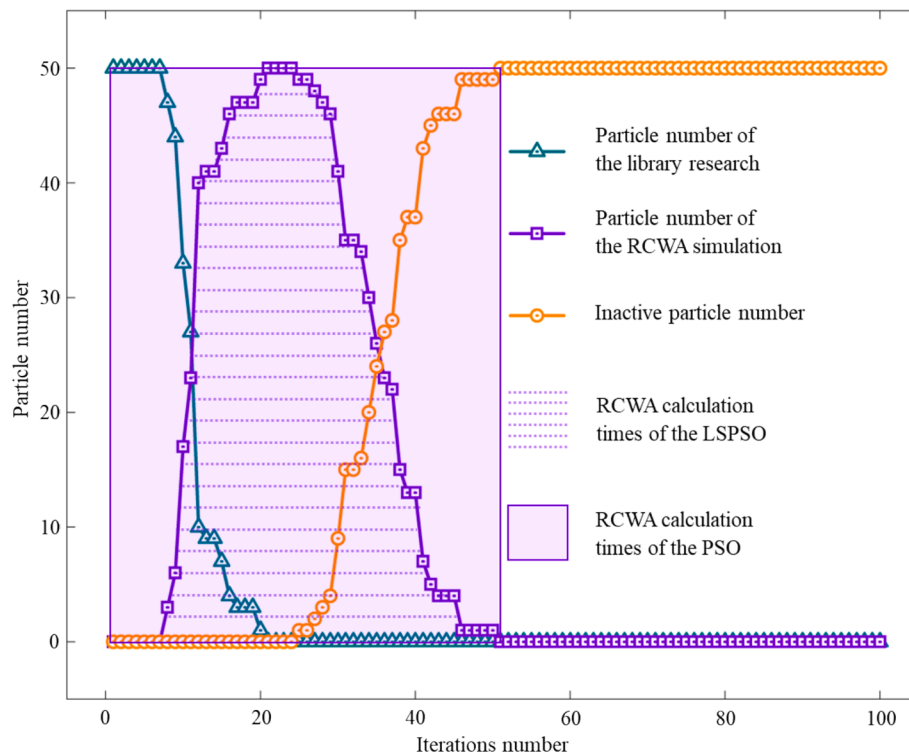


Fig. 10. Particle states with different search modes during multi-parameter Si grating measurement process.

algorithm's effectiveness in solving multi-dimensional problems.

Noisy experimental data in scatterometry require solution methods with high stability. To assess the noise robustness of the LSPSO algorithm, 20 % noise (relative to the reflectance values) was introduced into the reflectance data corresponding to 12 film and 8 grating models, as shown in Fig. 6. Previous studies have shown that this level of noise is representative of typical measurement and manufacturing errors [55–58]. When noisy data are used, both the film and grating models exhibit measurement errors, as depicted in Fig. 7. The simpler single-parameter optimization for film thickness results in smaller measurement errors (Fig. 7a) compared to the grating model (Fig. 7c). However, the root mean square error (RMSE) for the film model is noticeably higher than that for the grating model. This discrepancy arises because variations in film thickness induce larger changes in reflectance than variations in grating parameters, as confirmed by the data in Fig. 6. In conclusion, even under noisy conditions, the measurement errors for the film and grating models are constrained within 4 nm and 5 nm, respectively.

3.3. Experimental results

Simulation analysis has validated the accuracy of the LSPSO algorithm in solving both single-parameter and multi-parameter structures. However, the efficiency of LSPSO in problem-solving requires further experimental evaluation. The structure used in experiment is a multi-parameter Si grating structure, with parameters described in Section 3.2, including period P , height H , and width W . The grating structure was fabricated using an electron beam lithography (EBL) system, and the SEM images are shown in Fig. 8a and 8b. From the SEM top-view and cross-sectional images, it is evident that the grating structure fabricated by EBL has a clear profile, with only slight curvature at the etched bottom, almost perfectly matching the rectangular grating model. The grating morphology parameters were characterized using AFM, with a 3D scan view shown in Fig. 8c and 8d. To ensure that the nominal dimensions accurately describe the actual structure, these dimensions were determined by averaging measurements from multiple regions.

Profile line data were selected and calculated from 10 areas, resulting in the following actual grating parameters: $P = 125.2$ nm, $H = 63.8$ nm, and $W = 66.3$ nm.

The ARS results of the grating are shown in Fig. 9. Fig. 9a and 9b present the BFP images of the measured sample and the reference (bare silicon). The pixel intensities along the horizontal direction of the BFP images (indicated by the red rectangle) were extracted and normalized to obtain the angle-resolved reflectance. The raw reflectance data are shown in Fig. 9c, with the black curve representing the fitted data. To minimize the interference of noise in the raw data, appropriate data filtering methods were applied. The processed angle-resolved reflectance and the theoretical reflectance solved by the LSPSO algorithm are compared in Fig. 9d. At this point, the grating parameters that yielded the converged theoretical reflectance are: $P = 124$ nm, $H = 65$ nm, and $W = 64$ nm. The maximum error (compared to AFM characterization) occurred in parameter W , with an error value of 2.3 nm, corresponding to a measurement deviation of only 3.4 %. This demonstrates the reliability of the experimental ARS setup.

As previously mentioned, the advantage of the LSPSO algorithm lies in using a small spectral library to reduce the number of RCWA calculations, thereby improving the efficiency of the inverse problem-solving process. In this validation experiment, the three grating parameters were each varied within the ranges of 100 nm–150 nm, 40 nm–80 nm and 40 nm–80 nm, with a step size of 10 nm, to generate the LGI spectral library. Only 150 (6^*5^*5) pre-generated spectral data were required to achieve nanometer-level measurement accuracy. In contrast, using a strict library search method would require 150,000 (60^*50^*50) spectral data points. Compared to the library search method, LSPSO reduces the spectral data requirement by a factor of one thousand.

To evaluate the performance of the LSPSO algorithm in reducing RCWA calculations, the particle states at each search stage were statistically analyzed. The results are shown in Fig. 10. The area enclosed by the purple dashed and solid lines represents the number of times the RCWA model was called during the LSPSO algorithm iterations. The area enclosed by the purple dashed and solid lines represents the number of RCWA model calls during the iterations of the LSPSO algorithm,

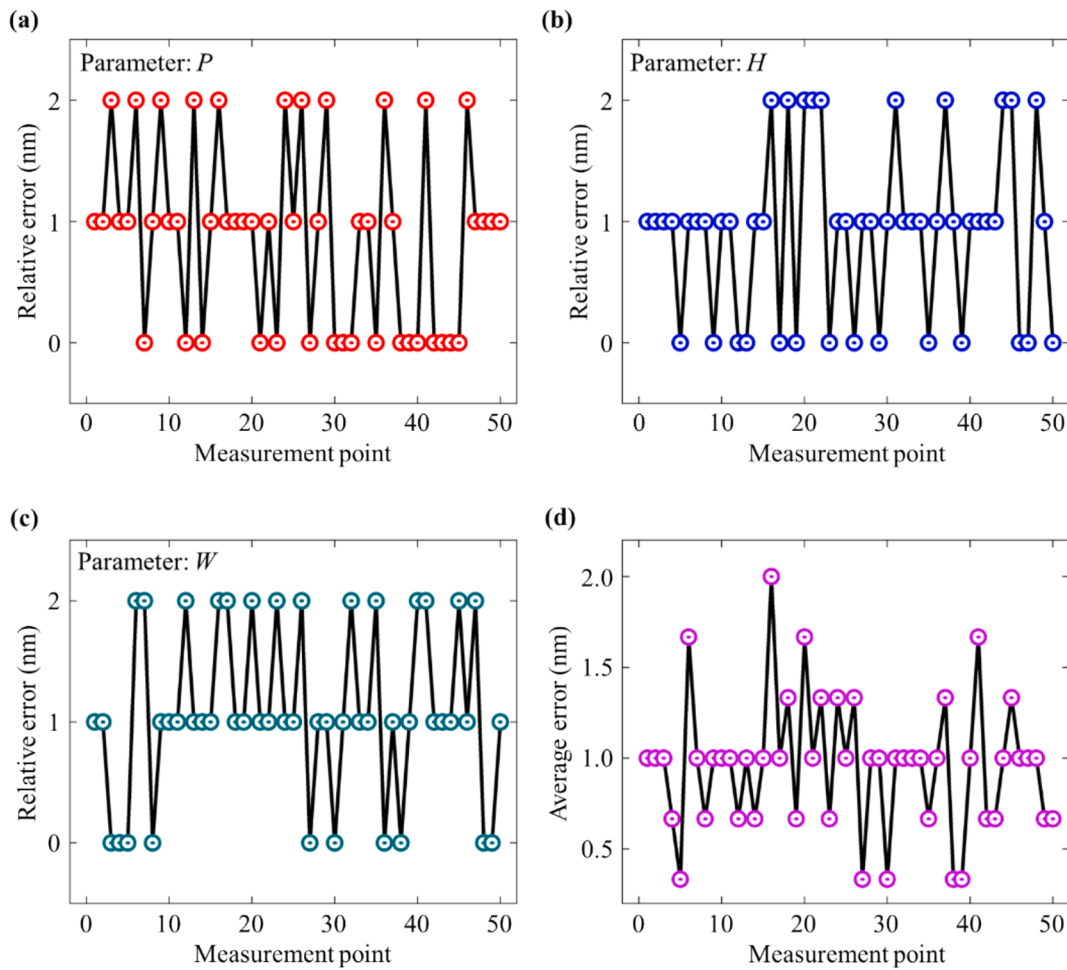


Fig. 11. The measurement results of LSPSO and LM. (a-c) relative measurement error between LSPSO and LM in P , H and W ; (d) the average relative measurement error of the three parameters.

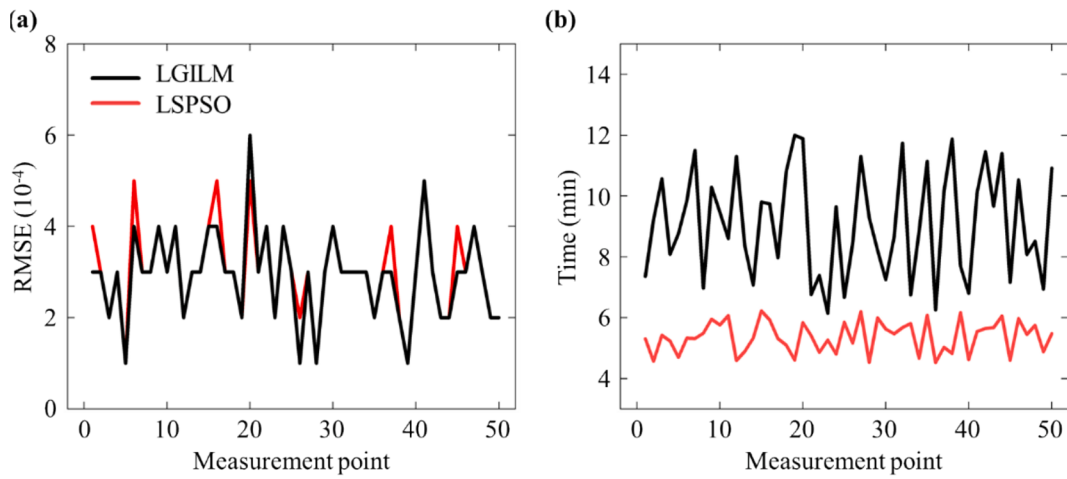


Fig. 12. Evaluation of solutions of LSPSO and LM. (a) the RMSE of LSPSO and LM; (b) the cost time of LSPSO and LM.

while the area of the purple rectangular box denotes the number of calls required by the traditional PSO algorithm. The LSPSO algorithm called the RCWA model 1,205 times, whereas the theoretical calculation for PSO would require 2,500 (50×50) calls, resulting in a 52 % improvement in solving efficiency. For higher dimensional parameters, the solving efficiency will be further improved, as more iterations are required to ensure solution accuracy.

A detailed comparison with the LGI-based LM (LGILM) method is conducted to further assess the performance of LSPSO. The grating structure was measured 50 times, and the results were solved using both methods. The relative errors for LSPSO and LGILM are presented in Fig. 11a-c. For all three CD parameters of the grating, the relative measurement errors for both methods remain within 2 nm. The average errors of the three parameters are further illustrated in Fig. 11d,

confirming the reliable accuracy of the LSPSO method. The RMSE for both methods are shown in Fig. 12a. Although LSPSO exhibits higher RMSE at specific points with larger measurement errors, its overall performance remains competitive. Notably, LSPSO significantly outperforms LGILM in computational efficiency across the entire measurement cycle (Fig. 12b). The average solution times for LSPSO and LGILM are 5.4 min and 9.1 min, respectively, indicating a 1.7-fold improvement in efficiency for LSPSO. This improvement can be attributed to differences in algorithmic complexity: unlike the LM method, PSO does not require gradient calculations, leading to substantially higher computational efficiency.

4. Conclusions

This study introduces a hybrid method combining library search and particle swarm optimization to improve the efficiency of inverse problem-solving in ARS. LSPSO addresses two major challenges: the high storage demands of spectral data in library search methods for multi-parameter measurements, and the computational inefficiency of real-time model evaluations in optimization algorithms. First, LSPSO utilizes an LGI library constructed with sparse spectral data, significantly reducing data volume compared to traditional library matching methods. Moreover, the LGI library guides the initial search process of the PSO, eliminating the need for model evaluations and further accelerating the optimization. Simulations demonstrated the algorithm's accuracy for both 12 film and 8 grating structures, with all results converging to the theoretical values. Stability was also verified in noisy data environments. Experimental evaluations on Si grating structures showed that LSPSO improves computational efficiency by 52 % compared to PSO and operates 1.7 times faster than the LGILM method. Additionally, LSPSO reduces the spectral data requirements to just 0.1 % of that required by traditional library search methods. These findings establish LSPSO as a highly efficient and resource-effective solution for ARS-based CD measurements.

Nonetheless, LSPSO's performance degrades in extreme noise environments, which is a common challenge in scattering measurements. Future work should focus on enhancing its noise resilience, such as incorporating redundant individuals in the particle population to mitigate the effects of measurement noise and improve algorithm robustness.

CRediT authorship contribution statement

Dekun Yang: Writing – original draft. **Wei Liang:** Writing – review & editing. **Shizhao Wang:** Data curation. **Wei Shen:** Writing – review & editing. **Jiantao Zhou:** Methodology. **Guanjun Wang:** Investigation. **Chong Shen:** Resources.

Declaration of competing interest

The authors declare that they have no known competing financial interests or personal relationships that could have appeared to influence the work reported in this paper.

Acknowledgments

This work was supported by Hainan Province Science and Technology Special Fund under Grant ZDYF2023GXJS005; Collaborative Innovation Center of Information Technology, Hainan University (XTCX2022XXB03); Major Program (JD) of Hubei Province (No. 2023BAA008); Jiangsu Province Engineering Research Center of Integrated Circuit Advanced Assembly and Test, China (No. NTIKFJJ202305); the Open Fund Project of the State Key Laboratory of Intelligent Vehicle Safety Technology (IVSTSKL-202308); Hainan University Research Initiation Fund Project (XJ2400011663).

Data availability

Data will be made available on request.

References

- [1] M.H. Madsen, P.E. Hansen, Scatterometry-fast and robust measurements of nano-textured surfaces, *Surf. Topogr. Metrol. Prop.* 4 (2016) 023003, <https://doi.org/10.1088/2051-672X/4/2/023003>.
- [2] V. Ferreras Paz, S. Peterhansel, K. Frenner, W. Osten, Solving the inverse grating problem by white light interference Fourier scatterometry, *Light Sci. Appl.* 1 (2012) e36, <https://doi.org/10.1038/lsci.2012.36>.
- [3] M.L. Gödecke, K. Frenner, W. Osten, Model-based characterisation of complex periodic nanostructures by white-light Mueller-matrix Fourier scatterometry, *Light, Adv. Manuf.* 2 (2021) 237–250.
- [4] C.J. Raymond, M.R. Murnane, S.L. Prins, S. Sohail, H. Naqvi, J.R. McNeil, J. W. Hosch, Multiparameter grating metrology using optical scatterometry, *J. Vac. Sci. Technol. B Microelectron. Nanom. Struct. Process. Meas. Phenom.* 15 (1997) 361–368, <https://doi.org/10.1116/1.589320>.
- [5] H.-T. Huang, F.L. Terry Jr, Spectroscopic ellipsometry and reflectometry from gratings (Scatterometry) for critical dimension measurement and in situ, real-time process monitoring, *Thin Solid Films* 455–456 (2004) 828–836, <https://doi.org/10.1016/j.tsf.2004.04.010>.
- [6] M.H. Madsen, P.-E. Hansen, Scatterometry—fast and robust measurements of nano-textured surfaces, *Surf. Topogr. Metrol. Prop.* 4 (2016) 023003, <https://doi.org/10.1088/2051-672X/4/2/023003>.
- [7] X. Chen, S. Liu, Optical Scatterometry for Nanostructure Metrology, in: 2019: pp. 477–513. DOI: 10.1007/978-981-10-4938-5_17.
- [8] M. Wurm, F. Pilarski, B. Bodermann, A new flexible scatterometer for critical dimension metrology, *Rev. Sci. Instrum.* 81 (2010), <https://doi.org/10.1063/1.3280160>.
- [9] C.J. Raymond, S.S.H. Naqvi, J.R. McNeil, Scatterometry for CD measurements of etched structures, in: S.K. Jones (Ed.), *Proc. SPIE - Int. Soc. Opt. Eng.*, 1996: pp. 720–728. DOI: 10.1117/12.240133.
- [10] S.H. Ye, S.H. Kim, Y.K. Kwak, H.M. Cho, Y.J. Cho, W. Chegal, Angle-resolved annular data acquisition method for microellipsometry, *Opt. Express* 15 (2007) 18056–18065, <https://doi.org/10.1364/oe.15.018056>.
- [11] S.H. Ye, Y.K. Kwak, S.H. Kim, H.M. Cho, Y.J. Cho, W. Chegal, D.G. Seiler, A.C. Diebold, R. McDonald, C.M. Garner, D. Herr, R.P. Khosla, E.M. Secula, Development of a focused-beam ellipsometer based on a new principle, in: *AIP Conf. Proc.*, AIP, 2007: pp. 69–73. DOI: 10.1063/1.2799439.
- [12] W.-D. Joo, J. You, Y.-S. Ghim, S.-W. Kim, Angle-resolved reflectometer for thickness measurement of multi-layered thin-film structures, in: *Interferom. XIV Tech. Anal.*, SPIE, 2008: pp. 245–252.
- [13] C. Guo, Y. Shi, H. Wu, Y. Xiang, W. Li, C. Zhang, S. Liu, A combination of library search and Levenberg-Marquardt algorithm in optical scatterometry, *Thin Solid Films* 767 (2023) 139670, <https://doi.org/10.1016/j.tsf.2023.139670>.
- [14] H. Ichikawa, Electromagnetic analysis of diffraction gratings by the finite-difference time-domain method, *J. Opt. Soc. Am. A* 15 (1998) 152–157, <https://doi.org/10.1364/JOSAA.15.000152>.
- [15] A.C. Polycarpou, Introduction to the Finite Element Method in Electromagnetics, *Synth. Lect. Comput. Electromagn.* 1 (2006) 1–126, <https://doi.org/10.2200/S00019EDV01Y200604CEM004>.
- [16] L. Li, New formulation of the Fourier modal method for crossed surface-relief gratings, *J. Opt. Soc. Am. A* 14 (1997) 2758–2767, <https://doi.org/10.1364/JOSAA.14.002758>.
- [17] S. Liu, Estimation of the convergence order of rigorous coupled-wave analysis for binary gratings in optical critical dimension metrology, *Opt. Eng.* 51 (2012) 081504, <https://doi.org/10.1117/1.OE.51.8.081504>.
- [18] V. Liu, S. Fan, S4 : A free electromagnetic solver for layered periodic structures, *Comput. Phys. Commun.* 183 (2012) 2233–2244, <https://doi.org/10.1016/j.cpc.2012.04.026>.
- [19] L. Wang, D. Fang, H. Jin, J. Li, 2D rigorous coupled wave analysis with adaptive spatial resolution for a multilayer periodic structure, *Opt. Express* 30 (2022) 21295–21308, <https://doi.org/10.1364/OE.459110>.
- [20] H. Contopanagos, B. Dembart, M. Epton, J.J. Ottusch, V. Rokhlin, J.L. Visher, S. M. Wandzura, Well-conditioned boundary integral equations for three-dimensional electromagnetic scattering, *IEEE Trans. Antennas Propag.* (2002), <https://doi.org/10.1109/TAP.2002.803956>.
- [21] Y.J. Liu, S. Mukherjee, N. Nishimura, M. Schanz, W. Ye, A. Sutradhar, E. Pan, N. A. Dumont, A. Frangi, A. Saez, Recent advances and emerging applications of the boundary element method, *Appl. Mech. Rev.* (2011), <https://doi.org/10.1115/1.4005491>.
- [22] P. Vincent, Differential methods, in: *Electromagn. Theory Gratings*, Springer, 1980: pp. 101–121.
- [23] K. Edee, J.P. Plume, J. Chandezon, On the Rayleigh-Fourier method and the Chandezon method: Comparative study, *Opt. Commun.* (2013), <https://doi.org/10.1016/j.optcom.2012.08.088>.
- [24] H. Gross, S. Heidenreich, M.A. Henn, M. Bär, A. Rathsfeld, Modeling aspects to improve the solution of the inverse problem in scatterometry, *Discret. Contin. Dyn. Syst. - Ser. S* (2015), <https://doi.org/10.3934/dcdss.2015.8.497>.
- [25] Scatterometry for Semiconductor Metrology, in: *Handb. Silicon Semicond. Metrol.*, CRC Press, 2001: pp. 389–418. DOI: 10.1201/9780203904541-25.

- [26] C.J. Raymond, M.E. Littau, A. Chuprin, S. Ward, Comparison of solutions to the scatterometry inverse problem, in: R.M. Silver (Ed.), *Metrol. Insp. Process Control Microlithogr.* XVIII, 2004: pp. 564–575. DOI: 10.1117/12.538662.
- [27] C. Raymond, Overview Of Scatterometry Applications In High Volume Silicon Manufacturing, in: AIP Conf. Proc., AIP, 2005: pp. 394–402. DOI: 10.1063/1.2062993.
- [28] X. Chen, S. Liu, C. Zhang, J. Zhu, Improved measurement accuracy in optical scatterometry using fitting error interpolation based library search, *Measurement* 46 (2013) 2638–2646, <https://doi.org/10.1016/j.measurement.2013.04.080>.
- [29] X. Chen, S. Liu, C. Zhang, H. Jiang, Improved measurement accuracy in optical scatterometry using correction-based library search, *Appl. Opt.* 52 (2013) 6726–6734, <https://doi.org/10.1364/AO.52.006726>.
- [30] J. Zhu, H. Jiang, Y. Shi, C. Zhang, X. Chen, S. Liu, Fast and accurate solution of inverse problem in optical scatterometry using heuristic search and robust correction, *J. Vac. Sci. Technol. b, Nanotechnol. Microelectron. Mater. Process. Meas. Phenom.* 33 (2015), <https://doi.org/10.1116/1.4919713>.
- [31] J. Elschner, G. Schmidt, M. Yamamoto, An inverse problem in periodic diffractive optics: global uniqueness with a single wavenumber, *Inverse Probl.* 19 (2003) 779–787, <https://doi.org/10.1088/0266-5611/19/3/318>.
- [32] J. Zhu, Y. Shi, L.L. Goddard, S. Liu, Application of measurement configuration optimization for accurate metrology of sub-wavelength dimensions in multilayer gratings using optical scatterometry, *Appl. Opt.* 55 (2016) 6844–6849, <https://doi.org/10.1364/AO.55.006844>.
- [33] R.C. Aster, B. Borchers, C.H. Thurber, *Parameter Estimation and Inverse Problems*, Elsevier (2019), <https://doi.org/10.1016/C2015-0-02458-3>.
- [34] T. Novikova, P. Bulkin, Inverse problem of Mueller polarimetry for metrological applications, *J. Inverse Ill-Posed Probl.* (2021), <https://doi.org/10.1515/jiip-2020-0140>.
- [35] C. Zhang, S. Liu, T. Shi, Z. Tang, Improved model-based infrared reflectometry for measuring deep trench structures, *J. Opt. Soc. Am. A* 26 (2009) 2327–2335, <https://doi.org/10.1364/JOSAA.26.002327>.
- [36] L.I. Goray, Solution of the inverse problem of diffraction from low-dimensional periodically arranged nanocrystals, *Model. Asp. Opt. Metrol. III* (2011), <https://doi.org/10.1117/12.889418>.
- [37] E. Baeyens, A. Herreros, J. Perán, A direct search algorithm for global optimization, *Algorithms* 9 (2016) 40, <https://doi.org/10.3390/a9020040>.
- [38] M. Juneja, S.K. Nagar, Particle swarm optimization algorithm and its parameters: A review, in: 2016 Int. Conf. Control. Comput. Commun. Mater., IEEE, 2016: pp. 1–5. DOI: 10.1109/ICCCM.2016.7918233.
- [39] W.H. Bangyal, J. Ahmad, H.T. Rauf, Optimization of neural network using improved bat algorithm for data classification, *J. Med. Imaging Heal. Informatics* (2019), <https://doi.org/10.1166/jmhi.2019.2654>.
- [40] W.H. Bangyal, J. Ahmad, I. Shafi, Q. Abbas, Forward only counter propagation network for balance scale weight & distance classification task, in: Proc. 2011 3rd World Congr. Nat. Biol. Inspired Comput. NaBIC 2011, 2011. DOI: 10.1109/NaBIC.2011.6089615.
- [41] S. Pervaiz, W.H. Bangyal, K. Nisar, N.U. Rehman, Population Initialization of Seagull Optimization Algorithm with Pseudo Random Numbers for Continous Optimization, in: Proc. - 2021 Int. Conf. Front. Inf. Technol. FIT 2021, 2021. DOI: 10.1109/FIT53504.2021.00019.
- [42] T.M. Luan, S. Khatir, M.T. Tran, B. De Baets, T. Cuong-Le, Exponential-trigonometric optimization algorithm for solving complicated engineering problems, *Comput. Methods Appl. Mech. Eng.* 432 (2024) 117411.
- [43] H.A. Abdushkour, M. Saadatmorad, S. Khatir, B. Benissa, F. Al Thobiani, A. U. Khawaja, Structural damage detection by derivative-based wavelet transforms, *Arab. J. Sci. Eng.* (2024) 1–9.
- [44] M. Saadatmorad, S. Khatir, T. Cuong-Le, B. Benissa, S. Mahmoudi, Detecting damages in metallic beam structures using a novel wavelet selection criterion, *J. Sound Vib.* 578 (2024) 118297.
- [45] A. Khatir, R. Capozucca, E. Magagnini, A. Oulad Brahim, A. Osmani, S. Khatir, L. Abualigah, Advancing structural integrity prediction with optimized neural network and vibration analysis, *J. Struct. Integr. Maint.* 9 (2024) 2390258.
- [46] B. Benissa, M. Kobayashi, M. Al Ali, S. Khatir, M. Shimoda, A novel exploration strategy for the YUKI algorithm for topology optimization with metaheuristic structural binary distribution, *Eng. Optim.* (2024) 1–21.
- [47] J. Kennedy, R. Eberhart, Particle swarm optimization (PSO), in: Proc. IEEE Int. Conf. Neural Networks, Perth, Aust., 1995: pp. 1942–1948.
- [48] J. Kennedy, R.C. Eberhart, A discrete binary version of the particle swarm algorithm, in: 1997 IEEE Int. Conf. Syst. Man, Cybern. Comput. Cybern. Simul., IEEE, 1997: pp. 4104–4108.
- [49] M. Settles, *An introduction to particle swarm optimization*, Dep. Comput. Sci. Univ. Idaho 2 (2005) 12.
- [50] X. Li, A.P. Engelbrecht, Particle swarm optimization: an introduction and its recent developments, in: Proc. 9th Annu. Conf. Companion Genet. Evol. Comput., 2007: pp. 3391–3414.
- [51] M. Juneja, S.K. Nagar, Comparative study of model order reduction using combination of PSO with conventional reduction techniques, in: 2015 Int. Conf. Ind. Instrum. Control. ICIC 2015, 2015: pp. 406–411. DOI: 10.1109/IIC.2015.7150776.
- [52] Q. Bai, Analysis of particle swarm optimization algorithm, *Comput. Inf. Sci.* 3 (2010) 180, <https://doi.org/10.5539/cis.v3n1p180>.
- [53] K.E. Parsopoulos, M.N. Vrahatis, Particle swarm optimization method in multiobjective problems, in: Proc. ACM Symp. Appl. Comput., 2002: pp. 603–607. DOI: 10.1145/508791.508907.
- [54] T. Zhang, P.F. Peng, K. Yang, D.D. Lei, Z.Y. Song, A Laplace sensitivity operator enhances the calculation efficiency of OCD metrology, *Opt. Express* 31 (2023) 2147–2160, <https://doi.org/10.1364/oe.475530>.
- [55] D. Yang, Z. Lei, L. Li, W. Shen, H. Li, C. Gui, Y. Song, High optical storage density using three-dimensional hybrid nanostructures based on machine learning, *Opt. Lasers Eng.* (2023), <https://doi.org/10.1016/j.optlaseng.2022.107347>.
- [56] Z. Lei, D. Yang, Y. Xu, H.A.Y. Song, C. Lei, Y. Zhao, Achieving ultra-high-density two-dimensional optical storage through angle resolved LSPR arrays: A case study of square array, *Opt. Commun.* (2023), <https://doi.org/10.1016/j.optcom.2023.129798>.
- [57] P. Zhang, F. Peng, D. Yang, Z. Lei, Y. Song, A Laplace sensitivity operator enhances the calculation efficiency of OCD metrology, *Opt. Express* (2023), <https://doi.org/10.1364/oe.475530>.
- [58] Q. Sun, D. Yang, T. Liu, J. Liu, S. Wang, S. Hu, S. Liu, Y. Song, Nondestructive monitoring of annealing and chemical-mechanical planarization behavior using ellipsometry and deep learning, *Microsystems Nanoeng.* (2023), <https://doi.org/10.1088/s41378-023-00529-9>.